

# Materials Research Express



## PAPER

# Thermomechanical buckling of boron nitride nanotubes using molecular dynamics

RECEIVED  
9 September 2015

REVISED  
21 November 2015

ACCEPTED FOR PUBLICATION  
4 December 2015

PUBLISHED  
20 January 2016

Anirban Chandra<sup>1</sup>, Puneet Kumar Patra<sup>2</sup> and Baidurya Bhattacharya<sup>3</sup>

<sup>1</sup> Department of Mechanical Engineering, Indian Institute of Technology Kharagpur, Kharagpur, India

<sup>2</sup> Advanced Technology Development Center, Indian Institute of Technology Kharagpur, Kharagpur, India

<sup>3</sup> Department of Civil Engineering, Indian Institute of Technology Kharagpur, Kharagpur, India

E-mail: [puneetpatra@atdc.iitkgp.ernet.in](mailto:puneetpatra@atdc.iitkgp.ernet.in) and [baidurya@civil.iitkgp.ernet.in](mailto:baidurya@civil.iitkgp.ernet.in)

**Keywords:** boron nitride nanotubes, thermo mechanical buckling, molecular dynamics, buckling

## Abstract

We study the thermal buckling behavior of precompressed boron-nitride nanotubes (BNNTs) using molecular dynamics simulations with Tersoff interatomic potential. We compute the critical buckling strains at near-zero temperature, and subsequently precompress the nanotubes at a certain fraction of this value followed by temperature ramping. The critical buckling temperature,  $T_{cr}$  is marked by a sudden decrease of the internal force. We observe that (i) at small to moderate lengths,  $T_{cr}$  is higher for chiral nanotubes than for either armchair or zigzag nanotubes, (ii)  $T_{cr}$  decreases with increasing diameter unlike in thermal disintegration where disintegration temperatures rise with increasing diameter, and (iii) armchair nanotubes have an optimal length for which  $T_{cr}$  is maximum. We qualitatively explain the reasons for each of the findings. Thermomechanical buckling occurs predominantly in two ways depending on the length of the nanotube—while the shorter nanotubes fail by radial instability (shell-like behavior), the longer ones invariably fail due to bending-buckling (rod-like behavior).

## 1. Introduction

Boron nitride nanotubes (BNNTs) have seen several applications over the last few years owing to their excellent mechanical strength [1, 2] and better chemical/thermal stability as compared to CNTs [3–6]. The good thermal and mechanical properties render it possible to use BNNTs in applications such as protective shielding for nanomaterials [7], hydrogen storage [8–10], sorption of gases [11], water purification [12], and fabrication of new composite materials [13]. As these devices become smaller, they dissipate a significant amount of heat over a small region [14]. Thus, the working conditions of BNNTs usually involve large stresses due to mechanical and thermal loadings, often both occurring simultaneously. It is therefore important to understand the structural response of BNNTs under not only independently applied mechanical or thermal load but also as under combined mechanical and thermal loads, a topic that has not received much attention.

The mechanical properties of BNNTs have been found using several different methods—molecular mechanics [2, 15, 16], molecular dynamics simulations [17, 18], first-principle studies [19, 20] and continuum modelling [21, 22]. All these studies indicate that the elastic and shear moduli of BNNTs are very high, almost comparable to CNTs. Although there is a significant dependence of mechanical properties on the chirality and the presence of defects (Stone-Wales and vacancies) [23, 24], the magnitude of the smallest of these remains very high—of the order of 100 GPa [23].

BNNTs can fail due to several reasons—yielding, defect propagation, material fracture, thermal disintegration, buckling etc. Their high yield strength [25, 26] and thermal disintegration temperatures [17] make BNNTs virtually impervious to failure due to independently applied mechanical or thermal loads. Among all failure modes, BNNTs are probably most susceptible to buckling. The buckling strength has been evaluated using classical molecular dynamics [27, 28], atomic scale finite element [29] and continuum approaches [22]. Buckling can occur either due to the separate action of mechanical or thermal stresses or due to a combination of

**Table 1.** Geometry of different nanotubes used in the study: indices ( $n, m$ ), diameter ( $D$ ) and total length ( $L_T$ ). Three different values of total lengths have been used.

$(n, m)$	$D$ (Å)	$L_{T,1}$ (nm)	$L_{T,2}$ (nm)	$L_{T,3}$ (nm)	Chiral Angle (°)
(10, 10)	13.8	6.9	13.8	20.7	30.0
(13, 7)	13.8	7.6	15.2	22.8	20.2
(15, 4)	13.8	7.5	15.0	22.5	11.5
(17, 0)	13.8	6.8	13.7	20.6	0.0

**Table 2.** Configuration of armchair nanotubes for investigating the effects of diameter.

$(n, m)$	$D$ (Å)	$L_T$ (nm)	$L$ (nm)	Chiral Angle (°)
(8, 8)	11.1	13.8	12.8	30.0
(10, 10)	13.8	13.8	12.8	30.0
(12, 12)	16.6	13.8	12.8	30.0
(15, 15)	20.7	13.8	12.8	30.0

both. The structural response of the BNNTs under buckling depends upon several factors; for example, with increasing tube diameter the critical buckling strain decreases significantly [30]. The buckling strength is also inversely proportional to the system temperature [28, 31].

However, the structural properties of the BNNTs under thermomechanical loading—that is, initially compressed BNNTs under progressively increasing thermal loading—have not yet been explored. In this paper we study the thermally assisted buckling of initially compressed BNNTs using classical molecular dynamics simulations. Our objectives are twofold: (i) assessment of critical buckling temperature ( $T_{cr}$ ), and (ii) identifying the mechanism and the governing structural variables determining  $T_{cr}$ . To accomplish our goals we study several BNNT configurations that elucidate the effects of chirality, length and diameter.

## 2. Modeling and simulation

### 2.1. Boron nitride nanotubes

A hexagonal boron nitride sheet comprises hexagonal ring-shaped structures in which each atom of nitrogen is bonded covalently to three boron atoms, and vice versa, with the nearest BN bond length being  $a = 1.4457$  Å [32]. Usually, a BNNT is characterized by three parameters: the chiral indices ( $n, m$ ) and the length,  $l$ . The diameter of a BNNT in terms of these parameters is

$$D = \frac{|C|}{\pi} = \frac{a}{\pi} \times \sqrt{3(m^2 + n^2 + mn)}, \quad (1)$$

and, the chiral angle can be computed as

$$\theta = \tan^{-1} \left( \frac{\sqrt{3}m}{2n+m} \right). \quad (2)$$

A chiral BNNT is denoted by a value of  $m$  that satisfies  $0 < m < n$ . A value of  $m = 0$  gives us a zigzag BNNT, while  $m = n$  gives an armchair BNNT. In the present study, we use 15 different nanotube configurations to gauge the effects of chirality, length and diameter. The BNNTs have been modelled using the nanotube builder tool of the open-source VMD package [33]. The geometrical parameters of the BNNTs used in the present study are shown in tables 1 and 2.

### 2.2. Interaction potential

The three-body Tersoff-like potential [34] has been adopted to model the interaction between the B-N atoms. The Tersoff potential can be expressed in the following form:

$$E = \sum_i E_i = \frac{1}{2} \sum_{i \neq j} \sum_j \phi(r_{ij}),$$

$$\phi(r_{ij}) = \sum_i \sum_{j>1} f_c(r_{ij}) [f_R(r_{ij}) + b_{ij} f_A(r_{ij})]. \quad (3)$$

In equation (3),  $r_{ij}$  is the distance between the  $i$ th and the  $j$ th atoms,  $b_{ij}$  is the bond order function,  $f_C$  denotes the cutoff function that ensures nearest-neighbor interaction,  $f_R$  denotes the repulsive pair potential, and  $f_A$  denotes the attractive pair potential. The mathematical forms of the individual functions are as follows:

$$\begin{aligned}
 f_C(r_{ij}) &= 1 && \forall r_{ij} < R_{ij} \\
 &= \frac{1}{2} - \frac{1}{2} \sin\left(\frac{\pi}{2} \times \frac{r_{ij} - R_{ij}}{S_{ij} - R_{ij}}\right) && \forall R_{ij} < r_{ij} < S_{ij} \\
 &= 0 && \forall r_{ij} > S_{ij} \\
 f_R(r_{ij}) &= Ae^{-\lambda_1 r_{ij}}, \\
 f_A(r_{ij}) &= -Be^{-\lambda_2 r_{ij}}, \\
 b_{ij} &= (1 + \beta^n \zeta_{ij}^n)^{-\frac{1}{2n}}, \\
 \zeta_{ij} &= \sum_{k \neq i, j} f_C(r_{ik}) g(\theta_{ijk}) \exp[\lambda_3^3 (r_{ij} - r_{ik})^3], \\
 g(\theta_{ijk}) &= 1 + c^2/d^2 - c^2/[d^2 + (h - \cos \theta_{ijk})^2].
 \end{aligned} \tag{4}$$

In expression (4),  $\theta_{ijk}$  is the angle between the bonds  $ij$  and  $ik$ . The parameters in the equation take different values depending upon the system being simulated. Several Tersoff potential parameters have been proposed for BN materials [36, 37]. In the present study we have used the parameters proposed by Sevik *et al* [37], which were obtained by fitting the simulation results to the structural, mechanical and vibrational characteristics of hexagonal BN. We were motivated to use this potential parameter set because of its widespread use [23, 44] and good agreement with results from first-principle studies and experiments [37, 38]. Previously, the same set of potential parameters has been used to estimate the thermal conductivity, vibrational frequencies and bending rigidity of BN systems at up to 1000 K [39, 44], making them suitable to investigate thermomechanical buckling characteristics.

### 2.3. Simulation mechanism

Molecular dynamics simulations were performed using the open-source LAMMPS package [40]. To understand the effect of thermomechanical buckling, a precompression is necessary. It must be noted, however, that the precompression force (or strain) should not be very high, or the system would buckle right away, and the thermal effects would be missed. Therefore, we have designed the simulations so that the nanotubes are compressed at a certain percentage of their buckling strain. Our definition of strain corresponds to engineering strain: the ratio of change in length of the system to the initial length of the system. The buckling load is calculated at (near ground state of) 0.1 K, and the corresponding strain is demarcated as the buckling strain. Subsequently, the temperature is ramped up until the nanotube buckles. These steps are explained next.

#### 2.3.1. Calculation of buckling load

The setup for calculating buckling load is shown in figure 1(a). The simulation domain is divided into three regions, depending upon the boundary conditions imposed. The bottommost region (the region marked 3 in figure 1(a)) is first fixed, and the resulting system is minimized using the conjugate gradient method to obtain a stable configuration. The rest of the boundary conditions are then imposed on this stable configuration—the topmost region (marked 1 in figure 1(a)) is constrained in such a manner that only displacement in the  $z$  direction is allowed, the central region (marked 2 in figure 1(a)) is allowed to move freely, and the bottommost region (marked 3 in figure 1(a)) is first fixed, and the resulting system is minimized using the conjugate gradient method to obtain a stable configuration. We are interested in the behavior of region 2, which has a free length of  $L$ . The region marked 3 is 5 Å long, while the length of the region marked 1 varies in such a manner that the free length (length of region 2) is kept fixed for a particular column of  $L_T$  (see table 1) in order to ensure uniformity.

The system is subjected to uniaxial compression by imposing a displacement rate of 0.1 Å/fs on region 1 along the  $z$ -direction. Each compression step is followed by 5,000 equilibration steps. Equilibration is performed at 0.1 K using the Nosé-Hoover thermostat [41]. The time step for performing numerical integration is 1 fs. During this equilibration, region 1 and region 3 are constrained in all directions whereas region 2 is free of any such constraints. The buckling load ( $P_{cr}$ ) is found by summing up the forces in the  $z$ -direction for all atoms within region 1. The critical strain ( $\epsilon_{cr}$ ) is taken as the strain at which  $P_{cr}$  occurs.

#### 2.3.2. Pre-compression followed by temperature ramping

The entire simulation is restarted, as highlighted in the previous subsection, but now the displacement is applied until the strain reaches a certain fraction  $\alpha$  of  $\epsilon_{cr}$ . In other words, rather than compressing the nanotube until (and beyond) buckling, we now apply a compressive load that is smaller than the buckling load. Every compression step is followed by 5000 equilibration steps at 0.1 K, as before. After compression, region 1 is

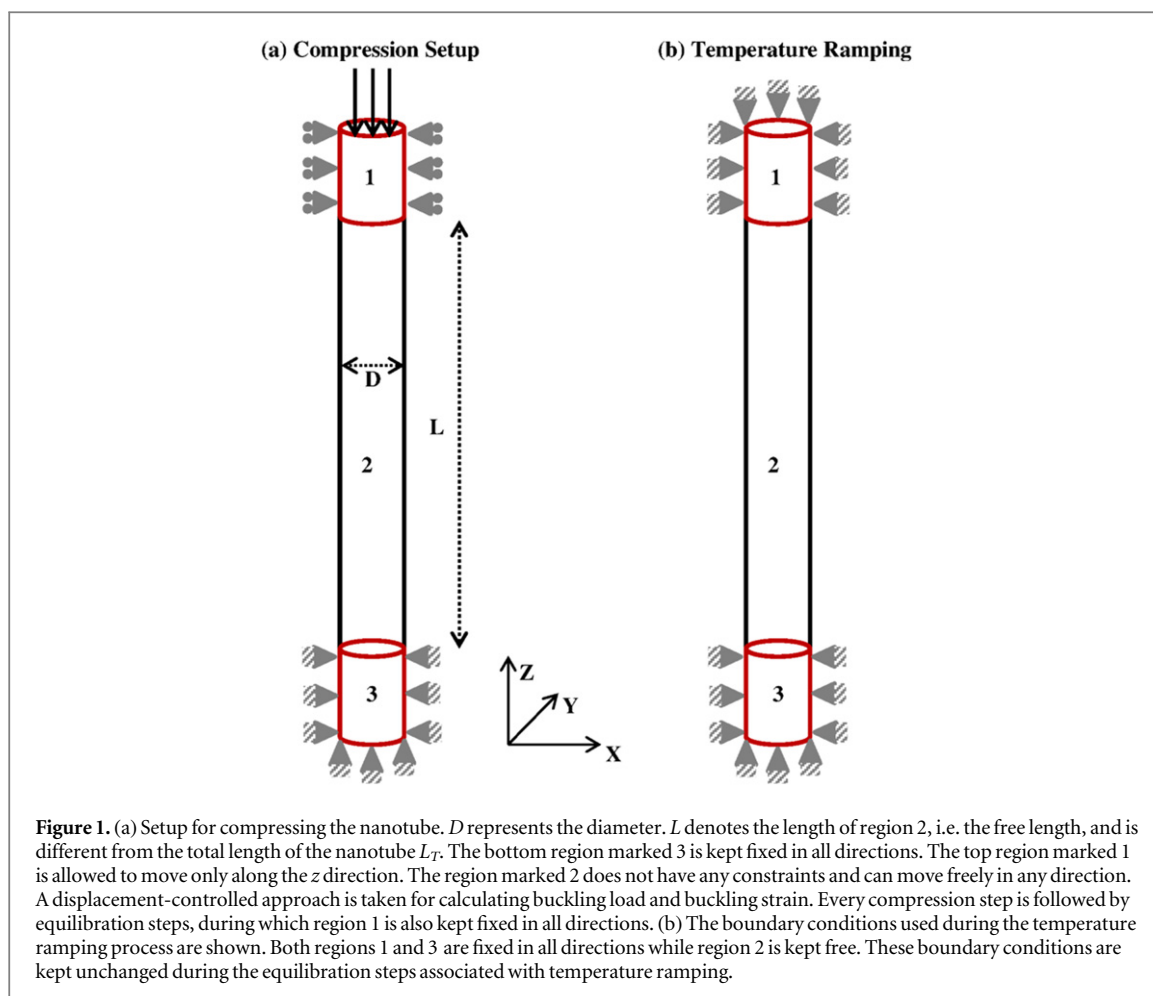


**Table 3.** Critical buckling load and critical strain for the different nanotubes of table 1.

(n, m)	$L_{T,1}$		$L_{T,2}$		$L_{T,3}$	
	$P_{cr}$ (nN)	$\epsilon_{CR}$	$P_{cr}$ (nN)	$\epsilon_{CR}$	$P_{cr}$ (nN)	$\epsilon_{CR}$
(10, 10)	61.99	0.058	52.22	0.047	39.00	0.038
(13, 7)	56.12	0.050	49.51	0.045	31.00	0.028
(15, 4)	56.46	0.051	49.65	0.045	30.20	0.028
(17, 0)	63.69	0.058	54.14	0.048	36.03	0.034

constrained along the  $z$ -direction. The temperature of the system is then ramped up at the rate of 10 K every fs. Each temperature ramping step is followed by 10000 equilibration steps. The boundary conditions employed during temperature ramping and the subsequent equilibration are portrayed in figure 1(b). Compressive forces are averaged over all the equilibration steps. The internal forces are then related to the temperature of the system to obtain the thermo-mechanical response of the system.

### 3. Results and discussions

The configurations of the different nanotubes used in the present study are detailed in tables 1 and 2. The values of  $(n, m)$  are chosen in such a way that the diameter of the nanotubes remains almost constant. The free lengths  $L$ , corresponding to the configurations given in table 1, are 5.9, 12.8 and 19.7 nm respectively. For investigating the effects of diameter only armchair nanotubes have been chosen (see table 2).

$P_{cr}$  and  $\epsilon_{cr}$  corresponding to the nanotubes of table 1 are shown in table 3. Just like in CNTs, [42], the buckling strength of BNNTs can be explained on the basis of bond configurations: (i) in zigzag nanotubes 1/3 of the bonds are along the loading direction and the compressing load transfers symmetrically over them, resulting in higher resistance to buckling; (ii) in chiral nanotubes none of the bonds are along the load-bearing direction or transverse to it, and due to the asymmetric nature of the bonds, the load is transferred asymmetrically, causing

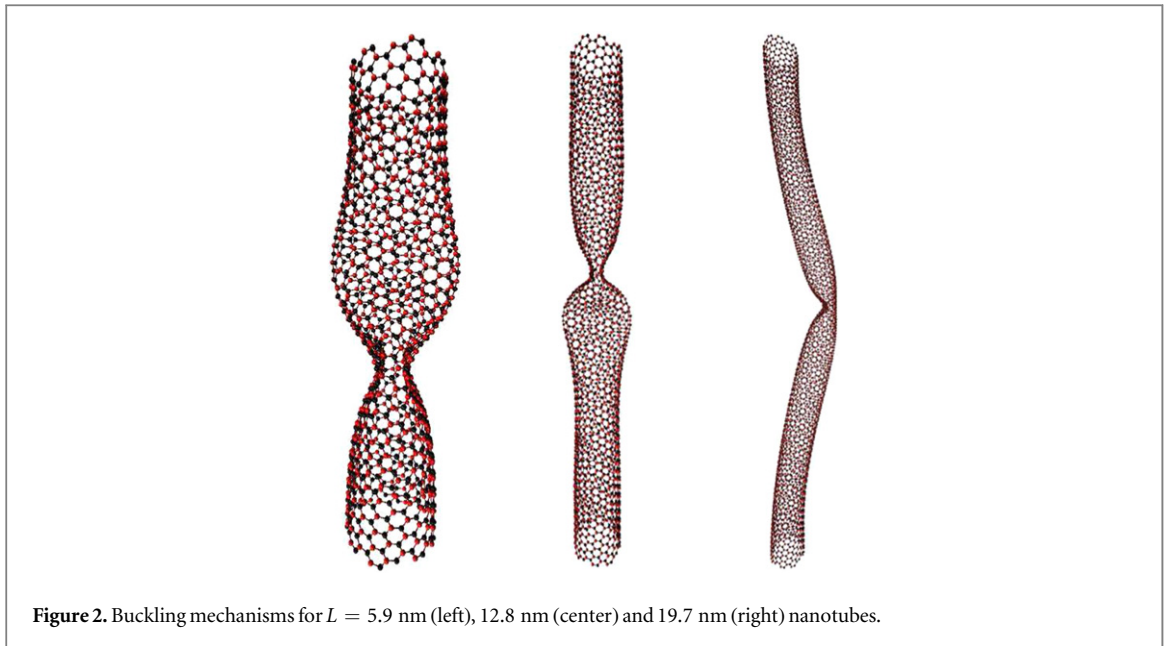


**Figure 2.** Buckling mechanisms for  $L = 5.9$  nm (left),  $12.8$  nm (center) and  $19.7$  nm (right) nanotubes.

**Table 4.** Critical buckling load and strain for different nanotubes shown in table 2.

(n, m)	$P_{cr}$ (nN)	$\epsilon_{CR}$
(8, 8)	44.49	0.052
(10, 10)	52.22	0.047
(12, 12)	56.40	0.043
(15, 15)	57.05	0.034

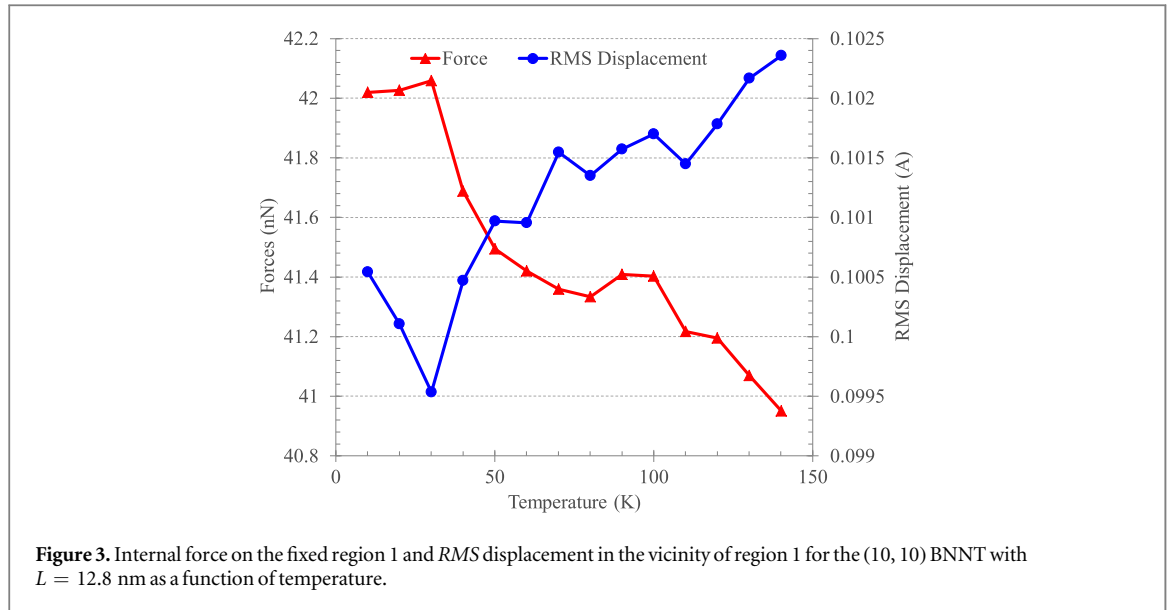
some bonds to displace more than others, eventually resulting in lower buckling loads; and (iii) in armchair nanotubes no bonds are along the loading direction, but the symmetric nature of the bonding allows symmetric load transfer, causing higher buckling strength than the chiral configurations. As is evident from the table, there is a significant dependence of both  $P_{cr}$  and  $\epsilon_{cr}$  on chirality and length. Short to moderately long zigzag nanotubes have the highest buckling strength. The buckling strength initially decreases as the chiral angle increases, but then increases as the armchair configuration is approached.

The buckling mechanism itself is independent of the chirality of the nanotubes but depends significantly upon their length—nanotubes with  $L \leq 12.8$  nm, regardless of their chirality, fail in radial buckling mode (see the left and center images of figure 2), and show limit point instability, while nanotubes with  $L = 19.7$  nm fail through excessive in-plane deformation, as seen typically in Euler struts, and exhibit rod-like behavior. This is subsequently followed by radial buckling (as typified in the right-hand image of figure 2). Despite the independence of the mechanism of buckling from chirality, the exact location at which the nanotubes buckle for different chiralities is not the same.

The mechanism of buckling is strongly influenced by the diameter of the nanotubes, at constant length. While BNNTs with  $D < 13.8$  Å show excessive in-plane deformation before radial buckling (like the bending-buckling as typified in figure 2 (right)), BNNTs with  $D \geq 13.8$  Å fail due to radial buckling (in a manner similar to the ones shown in figure 2 (left and center)). The buckling strength and strains for different nanotubes shown in table 2 are given in table 4.

The nanotube configurations shown in tables 1 and 2 are now subjected to the simulation setup detailed in the previous section. We choose  $\alpha = 0.7$ , i.e. the ratio of precompressing strain to the critical buckling strain,  $\epsilon_{cr}$ , is 0.7. The nanotubes undergo buckling as the temperature rises beyond a critical value, causing an abrupt decrease in internal axial force. The critical buckling temperature decreases with increasing  $\alpha$ .

It is interesting to note that as the temperature of the system is increased from near zero, the internal forces on region 1 decrease, unlike what has been observed in CNTs [42]. This decrease in the internal forces is due to the following reasons: (i) the negative coefficient of thermal expansion in BNNTs [43], and (ii) the instant the



temperature rises above 10 K, the BNNTs experience local radial expansion/contraction near region 1, resulting in a tensile effect on that region. Consequently, the internal compressive force decreases.

To validate the second hypothesis, we look at the average local expansion/contraction as a function of temperature near the vicinity of region 1. Local aberration is obtained by calculating the RMS displacement of the atoms with respect to their mean positions at near ground state,  $(x_0, y_0, z_0)$ . It is seen that the atoms in the vicinity of region 1 move away from their ground-state positions (along the axis of the nanotube) as the temperature is increased, providing a net tension on region 1. This eventually results in a decrease of the net compressive force on it.

$$\text{RMS} = \sqrt{\frac{1}{N} \sum_i [(x_i - x_0)^2 + (y_i - y_0)^2 + (z_i - z_0)^2]} \quad (5)$$

The results for RMS are highlighted in figure 3. Notice the inverse relation between the force and RMS displacement—internal force increases when the displacement decreases and vice versa, validating our reasoning.

### 3.1. Effects of chirality

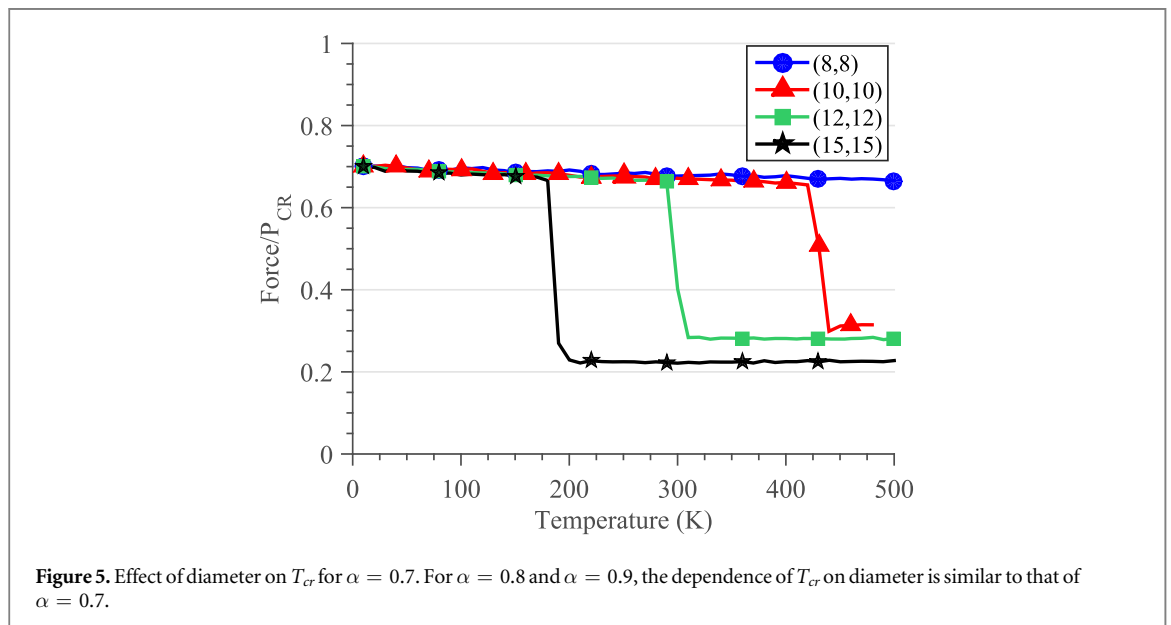
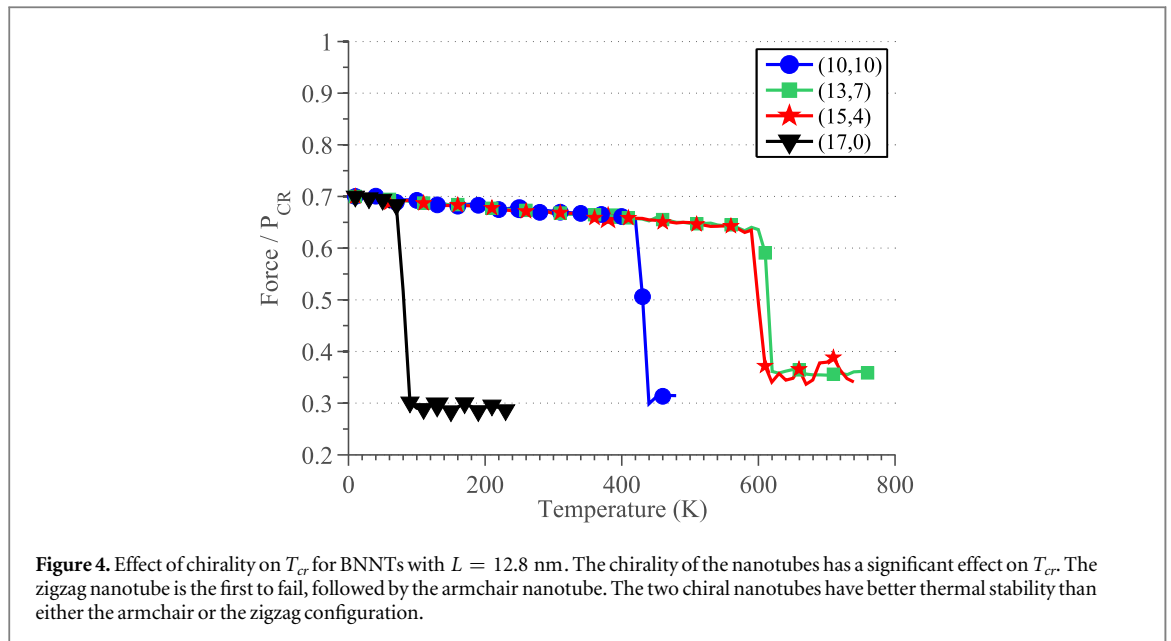
The armchair and zigzag BNNTs are expected to have an inferior thermo-mechanical response as compared to the chiral BNNTs due to the inherent symmetry in their structures, which amplifies thermal perturbations. The armchair configuration is comparatively more stable than the zigzag because 1/3 of the former's bonds are aligned transverse to the loading direction, and thus have more resistance to radial buckling caused by local perturbations. None of the bonds in the zigzag BNNTs are aligned perpendicular to the loading direction, and all of them are in compression. A combination of these factors makes them very unstable against radial fluctuations.

To elaborate this effect, an artificial radial imperfection is introduced in precompressed BNNTs at 10 K and then further compression is applied. It is seen that when the amplitude of the radial imperfection exceeds a certain value, the zigzag BNNT fails immediately while the armchair BNNT absorbs the imperfection, regains its original configuration and eventually buckles at a much higher mechanical load. If, however, the amplitude is significantly large then the armchair BNNT also fails as soon as the defect is introduced. The primary effect of temperature loading on BNNTs is the introduction of these kinds of 'multiple' local radial imperfections. Moreover, as the temperature increases, the amplitude of the radial imperfections also increases.

The results for  $L = 12.8$  nm BNNTs for  $\alpha = 0.7$  are shown in figure 4. The results are as per our expectations—the armchair configuration has higher  $T_{cr}$  than the zigzag configuration, and the highest thermal stability is exhibited by the chiral BNNTs. The asymmetrical bonding of the chiral BNNTs inhibits the amplification of thermal perturbations and thus they are least susceptible to thermal buckling. The higher buckling temperature of the (15, 4) BNNT than the (13, 7) BNNT suggests that  $T_{cr}$  increases with decrease in chiral angle.

### 3.2. Effect of diameter at constant length and fixed chirality

The effect of diameter (at constant  $L = 12.8$  nm) on the  $T_{cr}$  is similar to the one observed for CNTs—as the diameter increases, the  $T_{cr}$  decreases. For simplicity, only armchair configurations have been considered in this study. This is in contrast to the thermal disintegration of the BNNTs, where the disintegration temperature



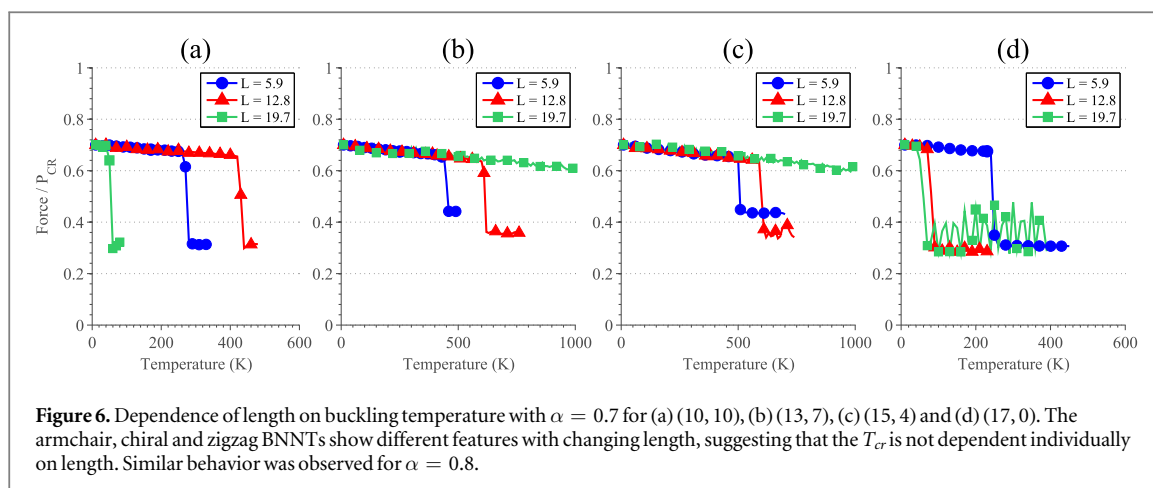
increases with increasing radius due to the lower strain energy density of the wider BNNTs [17]. Figure 5 shows the values of  $T_{cr}$  when  $\alpha = 0.7$ .

It is interesting to note that all BNNTs except (8, 8) fail due to radial buckling. The (8, 8) BNNT undergoes bending-buckling failure and fails at a higher  $T_{cr}$  than the rest. At lower load factors bending is induced in the (8, 8) BNNT only after the temperature rises beyond a substantial value, and the bending is followed by radial buckling. Consequently, at these load factors, (8, 8) shows the highest resistance to thermal buckling.

### 3.3. Effect of length

To understand the effect of length let us look at figure 6, which shows the thermo-mechanical buckling behavior of (10, 10), (13, 7), (15, 4) and (17, 0) BNNTs for  $\alpha = 0.7$ . The longest BNNT ( $L = 19.7$  nm) invariably fails by bending-buckling, while the shortest ones fail due to radial buckling. The medium-length BNNTs may undergo either of the above or a combination of the two.

Figure 6 shows that the  $L = 12.8$  nm (10, 10) BNNT fails at a much higher temperature than either the shorter 5.9 nm BNNT or the longer 19.7 nm BNNT. This suggests that the armchair (10, 10) configuration has an optimum length for which  $T_{cr}$  reaches a maximum — as  $L$  increases,  $T_{cr}$  increases, attains a maximum value, and subsequently decreases. This is because the local thermal perturbations generated in the 5.9 nm armchair BNNT affect the system globally due to its small axial dimension and, therefore, it fails the earliest. The 12.8 nm



BNNT, being longer, can reduce the global effects of the local perturbations, resulting in a higher buckling temperature. On the other hand the longest BNNT undergoes bending-buckling, and thus fails earlier than the 12.8 nm BNNT.

The length dependence for the zigzag nanotube follows the common expectation — as length increases, the  $T_{cr}$  decreases. The 5.9 nm and 13.8 nm zigzag BNNTs undergo radial buckling at lower temperatures as compared to their armchair and chiral counterparts. Further, the longer 19.7 nm BNNT undergoes bending failure at a temperature lower than the above two. As length increases, the number of local imperfections being created also increases. This, combined with the fact that zigzag nanotubes do not have significant resistance to radial instabilities, makes them fail progressively earlier with increasing length.

For chiral nanotubes we see that with increasing length,  $T_{cr}$  increases. The chiral 19.7 nm BNNTs at lower loads do not show any bending, and thus do not fail at temperatures up to 1000 K. However as the load is increased, a rapid decrease in the  $T_{cr}$  is observed since the nanotube bending becomes prominent at higher loads. The 12.8 and 5.9 nm BNNTs show deformation characteristics that depend on the chiral angle.

#### 4. Conclusions

The predominant effect of thermal loading is the creation of multiple local imperfections because of which the nanotubes have a ‘wavy’ structure. Counterintuitively, these local imperfections lead to a reduction in the internal forces of the system, on account of their tensile effect on the fixed ends. Despite the decrease in the internal forces, the critical buckling temperature,  $T_{cr}$ , is well defined.

Chirality has a significant influence on the  $T_{cr}$ —chiral nanotubes fail at a much higher temperature than either armchair or zigzag nanotubes. We attribute this to the asymmetrical bond profile of the chiral nanotubes. The local thermal imperfections arising due to the increase in temperature aid in buckling. However, the asymmetrical bonding of the chiral BNNTs hinders the amplification of these thermal perturbations, which makes them less susceptible to buckling. The symmetric structure of the zigzag nanotubes and the fact that all their bonds are under compression make them most susceptible to buckling induced by thermal vibrations. For armchair nanotubes, although the bonding is symmetric, since 1/3 of their bonds (the horizontal bonds) are in tension, they have more resistance to buckling due to locally created imperfections. However, because of the symmetry, they buckle faster than the chiral nanotubes. We also observe that the  $T_{cr}$  increases with decreasing chiral angle.

Armchair BNNTs with smaller radii tend to undergo bending-buckling while the ones with larger radii fail predominantly by radial buckling. At small values of  $\alpha$ , where sufficiently large bending is not induced in the nanotube, the shorter-radius BNNT fails at the highest temperature. This behavior changes at large values of  $\alpha$ , where shorter-radius BNNTs fail the fastest. The effect of diameter can be summarized in a single statement as, when diameter increases, buckling temperature decreases at small to moderate precompression strains. Interestingly, the effect of the length of the nanotubes is intrinsically coupled to the precompression strain,  $\alpha$ , as well as to chirality.

#### References

- [1] Garel J, Leven I, Zhi C, Nagapriya K, Popovitz-Biro R, Golberg D, Bando Y, Hod O and Joselevich E 2012 *Nano Lett.* **12** 6347–52

- [2] Santosh M, Maiti P K and Sood A K 2009 *J. Nanoscience Nanotechnology* **9** 5425–30
- [3] Han W Q, Mickelson W, Cumings J and Zettl A 2002 *Appl. Phys. Lett.* **81** 1110–2
- [4] Golberg D, Bando Y, Tang C and Zhi C 2007 *Adv. Mater.* **19** 2413–32
- [5] Chen Y, Zou J, Campbell S J and Le Caer G 2004 *Appl. Phys. Lett.* **84** 2430–2
- [6] Blase X, Rubio A, Louie S G and Cohen M L 1994 *Europhys. Lett.* **28** 335
- [7] Li Y, Dorozhkin P, Bando Y and Golberg D 2005 *Adv. Mater.* **17** 545–9
- [8] Wu X, Yang J, Hou J G and Zhu Q 2006 *J. Chem. Phys.* **124** 054706
- [9] Mpourmpakis G and Froudakis G E 2007 *Proc. of the Korea Conf. on Innovative Science and Technology (KCIST-2005) Frontiers in Hydrogen Storage Materials and Technology Catal. Today* **120** 341–5
- [10] Ma R, Bando Y, Zhu H, Sato T, Xu C and Wu D 2002 *J. Am. Chem. Soc.* **124** 7672–3
- [11] Ganji M D, Mirnejad A and Najafi A 2010 *Sci. Technol. Adv. Mater.* **11** 045001
- [12] Lei W, Portehault D, Liu D, Qin S and Chen Y 2013 *Nat. Commun.* **4** 1777
- [13] Zhi C, Bando Y, Tang C, Honda S, Kuwahara H and Golberg D 2006 *J. Mater. Res.* **21** 2794–800
- [14] Cao G, Chen X and Kysar J W 2006 *J. Mech. Phys.* **54** 1206–36
- [15] Yang J E, Hong Y T and Lee J S 2006 *J. Nanoscience Nanotechnology* **6** 3594–8
- [16] Theodosiou T C and Saravanos D A 2011 *Int. J. Comput. Methods Eng. Sci. Mech.* **12** 203–11
- [17] Moon W H and Hwang H J 2004 *Nanotechnology* **15** 431
- [18] Liao M L, Wang Y C, Ju S P, Lien T W and Huang L F 2011 *J. Appl. Phys.* **110** 054310
- [19] Kinoshita Y and Ohno N 2010 *Phys. Rev. B* **82** 085433
- [20] Fakhrabad D V and Shahtahmassebi N 2013 *Mater. Chem. Phys.* **138** 963–6
- [21] Oh E S 2010 *Mater. Lett.* **64** 859–62
- [22] Song J, Wu J, Huang Y and Hwang K C 2008 *Nanotechnology* **19** 445705
- [23] Anoop Krishnan N M and Ghosh D 2014 *J. Appl. Phys.* **115** 064303
- [24] Vaccarini L, Goze C, Henrard L, Hernandez E, Bernier P and Rubio A 2000 *Carbon* **38** 1681–90
- [25] Hernández E, Goze C, Bernier P and Rubio A 1998 *Phys. Rev. Lett.* **80** 4502–5
- [26] Huang Y, Lin J, Zou J, Wang M S, Faerstein K, Tang C, Bando Y and Golberg D 2013 *Nanoscale* **5** 4840–6
- [27] Shokuhfar A and Ebrahimi-Nejad S 2013 *Physica E* **48** 53–60
- [28] Ebrahimi-Nejad S and Shokuhfar A 2013 *Physica E* **50** 29–36
- [29] Tao J, Xu G and Sun Y 2015 *Mathematical Problems in Engineering* **2015** 240547
- [30] Akdim B, Pachter R, Duan X and Adams W W 2003 *Phys. Rev. B* **67** 245404
- [31] Shokuhfar A, Ebrahimi-Nejad S, Hosseini-Sadegh A and Zare-Shahabadi A 2012 *Phys. Status Solidi a* **209** 1266–73
- [32] Rubio A, Corkill J L and Cohen M L 1994 *Phys. Rev. B* **49** 5081–4
- [33] Humphrey W, Dalke A and Schulten K 1996 *J. Mol. Graph.* **14** 33–8
- [34] Tersoff J 1989 *Phys. Rev. B* **39** 5566–8
- [35] Verma V, Jindal V K and Dharamvir K 2007 *Nanotechnology* **18** 435711
- [36] Sekkal W, Bouhafs B, Aourag H and Certier M 1998 *J. Phys.: Condens.* **10** 4975
- [37] Sevik C, Kinaci A, Haskins J B and Çğın T 2011 *Phys. Rev. B* **84** 085409
- [38] Kinaci A, Haskins J B, Sevik C and Çğın T 2012 *Phys. Rev. B* **86** 115410
- [39] Singh S K, Neek-Amal M, Costamagna S and Peeters F M 2013 *Phys. Rev. B* **87** 184106
- [40] Plimpton S 1995 *J. Comput. Phys.* **117** 1–9
- [41] Hoover W G 1985 *Phys. Rev. A* **31** 1695–7
- [42] Zhang Y Y, Tan V B C and Wang C M 2006 *J. Appl. Phys.* **100** 074304
- [43] Mashreghi A 2012 *Comput. Mater. Sci.* **65** 356–64
- [44] Chandra A, Patra P K and Battacharya B 2015 *J. Appl. Phys.* **118** 234503